Operation mechanism in hybrid Mg-Li batteries with $TiNb_2O_7$ allowing stable high-rate cycling

Sebastian Maletti,[a] Oleg Janson,[a] Abraham Herzog-Arbeitman[a,b], Ignacio Guillermo Gonzalez Martinez,[a] Ronny Buckan,[a] Johanna Fischer,[a] Anatoliy Senyshyn,[c] Alexander Missyul,[d] Martin Etter,[e] Daria Mikhailova[a*]

[a] Leibniz Institute for Solid State and Materials Research (IFW) Dresden e.V., Helmholtzstraße 20, D-01069 Dresden, Germany

[b] Department of Chemistry, University of Chicago, Chicago, Illinois 60637, United States

[c] Forschungsneutronenquelle Heinz Maier-Leibnitz FRM-II, Technische Universität München, Lichtenbergstr. 1, D-85747 Garching bei München, Germany

[d] ALBA Synchrotron Light Source, Carrer de la Llum 2-26, 08290 Cerdanyola del Vallès, Barcelona, Spain

[e] Deutsches Elektronen-Synchrotron (DESY), Notkestraße 85, D-22607 Hamburg, Germany

Corresponding Email: d.mikhailova@ifw-dresden.de

Keywords: Beyond lithium batteries concept, dual salt batteries, pseudocapacitive storage, fast Mg deposition/stripping, Wadsley-Roth phase, Li,Mg co-intercalation, cathode electrolyte interface

ABSTRACT

We studied the structural evolution and cycling behavior of $TiNb_2O_7$ (TNO) as cathode in a non-aqueous hybrid dual-salt Mg-Li battery. A very high fraction of a pseudocapacitive contribution to the overall specific capacity makes the material suitable for ultrafast operation in a hybrid battery, comprised of a Mg-metal anode, and a dual-salt APC-LiCl electrolyte with Li and Mg cations. Theoretical calculations show that Li-intercalation is predominant over Mg-intercalation into the TNO in a dual-salt electrolyte with Mg^{2+} and Li^+, while experimentally up to 20% Mg-co-intercalation was observed after battery discharge.

In hybrid Mg-Li batteries, TNO shows capacities which are about 40 mAh g^{-1} lower than in single-ion Li-batteries at current densities up to 1.2 A g^{-1}. This is likely due to a partial Mg co-intercalation, or/and location of Li-cations on alternative crystallographic sites in the TNO structure in comparison to Li-intercalation process in Li-batteries. Generally, hybrid Mg-Li cells show a markedly superior applicability for a very prolonged operation (above 1000 cycles) with 100% Coulombic efficiency and a capacity retention higher than 95% in comparison to conventional Li-batteries with TNO after being cycled either under a low (7.75 mA g^{-1}) or high (1.55 A g^{-1}) current density.

The better long-term behavior of the hybrid Mg-Li batteries with TNO is especially pronounced at 60 °C. The reasons for this are an appropriate cathode electrolyte interface containing $MgCl_2$-species as well as a superior performance of the Mg-anode in APC-LiCl electrolytes with a dendrite-free, fast Mg deposition/stripping. This stable interface stands in contrast to the anode electrolyte interface in Li-batteries with a Li-anode in conventional carbonate-containing electrolytes, which is prone to dendrite formation, thus leading to a battery shortcut.

INTRODUCTION

The transformation of today's energy storage landscape to more powerful and sustainable technologies involves a large number of well-developed battery concepts, such as the next-generation Lithium-Ion Batteries (LIBs), Sodium-Ion Batteries (SIBs) and Lithium-Sulfur Batteries. Another approach, which is still under development, is the concept of Hybrid Batteries based on reactions of two metal cations. This is of particular interest for the use of multivalent ions, such as Mg^{2+}, since a breakthrough on the viability of pure multivalent batteries is not expected soon.[1,2] Especially, Mg-Li hybrid batteries (MLHBs) with promising electrochemical properties have been reported. Their main advantage is the use of a magnesium metal anode, which provides a very high energy density and is considered safe due to non-dendritic deposition of Mg. As positive electrodes, mainly Mo_6S_8,[3,4] TiO_2,[5] FeS_x[6] and TiS_2[7] have been applied successfully with „All-Phenyl Complex" (APC) electrolytes based on $(PhMgCl)_2$-$AlCl_3$ and a Li salt, such as LiCl or $LiBH_4$. Although these systems restrict the operating voltage of MLHBs to a narrow electrochemical window, promising results in terms of capacity and long-term stability have been demonstrated.

Despite the large number of related studies, the charge storage mechanism taking place at the positive electrode in MLHBs remains dimly understood. Often, it is simply assumed that Li^+ is inserted selectively because of its lower charge as compared to Mg^{2+}, which results in enhanced diffusivity. In fact, the situation remains quite vague, since both ions have comparable sizes (0.76 Å for Li^+ *vs.* 0.72 Å for Mg^{2+} in an octahedral oxygen surrounding)[8] and it is not fully clear how charge and size determine the insertion behavior. In addition to factors inherent to the cations, properties of the host material should influence cation insertion, especially the availability of intercalation sites and the geometry of pathways. Apart from the simplification that Li^+ should always be preferred over Mg^{2+} because of its lower charge, a number of studies has found that a co-insertion occurs; for instance, in Mo_6S_8[4], $Li_4Ti_5O_{12}$[9], or $MgCo_2O_4$[10]. It may also happen that the insertion of Li^+ facilitates the uptake of Mg, e.g. by expanding interlayers or diffusion channels.

$TiNb_2O_7$ (TNO) belongs to the Wadsley-Roth oxide family,[11] adopting a tunnel-like crystal structure of the ReO_3 type with different connections of metal-oxygen polyhedra that allow a quasi 3D diffusion of guest ions (Figure 1). However, completely unhindered cation motion in TNO occurs solely along the *b*-axis.[12] Visualization of possible diffusion pathways for metal cations in the TNO structure shows equal options for Li^+ and Mg^{2+} (Figure 1), suggesting no geometrical limits for co-intercalation of these metals. In a previous report,[13] the activation barriers for cation diffusion for Li, Na, K, and Mg were estimated using DFT calculations. It was found out that for all cations heavier than Li, the diffusion barriers along the *b*-axis are considerably larger than the corresponding Li barriers: $\Delta E(Li^+) \ll \Delta E(Mg^{2+}) < \Delta E(Na^+) \ll \Delta E(K^+)$. This finding, however, points only to a kinetic obstacle for cation diffusion, since a reversible Na-insertion and removal into/from nano-scaled TNO has been reported elsewhere[14]. Therefore, Mg-intercalation into a nano-structured TNO might not be ruled out.

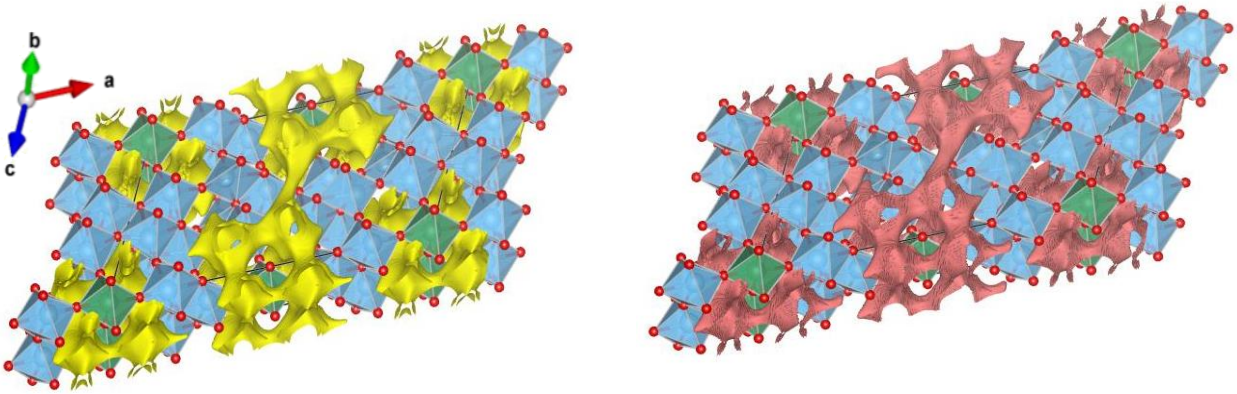

Figure 1. Differential bond-valence sums[15] for Li (left, yellow color) and Mg (right, brownish color) cations in the $TiNb_2O_7$ structure, performed using the Software *VESTA 3*.0.[16] Ti and Nb cations are randomly distributed in blue octahedra while mostly Ti cations occupy green octahedra.

After incorporating into an electronically conductive network, TNO[17] demonstrates superior anodic properties in Li-batteries that are comparable to well-known $Li_4Ti_5O_{12}$ anode material. Further, a stable cycling at a current density of 1935 mA g^{-1} with capacities about 200 mAh g^{-1} and 84% capacity retention after 1000 cycles was reported for nanoporous TNO[10], whereas the capacity of 260 mAh g^{-1} at 387 mA g^{-1} was shown for TNO nano-fibers for 50 cycles.[18]

The outstanding intercalation properties of TNO originate from the nano-scale morphology[17] which facilitates Li^+ insertion and extraction and provides a fast electron transfer pathway, thus enabling high-performance lithium ion pseudocapacitive behavior.

Previous work on $TiNb_2O_7$ electrodes in hybrid Mg-Li batteries showed a principal functional window between -10 °C and +60 °C with an APC electrolyte containing LiCl as a Li-source. The capacities achieved are slightly lower than these of Li-batteries, but with a much more stable cycling behavior at moderate rates.[19] The origin of the increased cycling stability could be partially explained by a convenient solid-electrolyte interface containing highly conductive chlorides, which forms on the powdered $TiNb_2O_7$ electrode in hybrid batteries.

However, two more issues can contribute to the stable cyclability of Mg-Li hybrid batteries, namely *i*) the storage mechanism in TNO, and *ii*) the enhanced stability of the Mg-anode *vs*. Li-anode, especially under extreme conditions such as high current density and/or temperature. In our previous work, a large pseudocapacitive contribution to the total specific capacity in the Mg-Li hybrid battery was demonstrated[19] which is similar to the Li-cells.[17] However, the structural changes in the TNO-cathode in Mg-Li hybrid cells, caused by the cation intercalation, must still be clarified. Hence, first using DFT calculations we examined a thermodynamic probability for Mg-insertion into $TiNb_2O_7$ by comparison of energies of the Li- and Mg-intercalated TNO phases. Next, the insertion mechanism into TNO in hybrid batteries was investigated in details using *operando* XRD, *operando* XAS, and *post mortem* TEM studies. Finally, we performed long-term cycling of TNO in Li- and hybrid Mg-Li cells at very high current densities, and compared the stability of Li-and Mg-anodes in symmetrical cells using appropriate Li- and Mg-Li electrolytes. The performed studies allowed to understand the enhanced cycling stability of Mg-Li hybrid cells with TNO in comparison to Li-cells.

MATERIALS AND METHODS

Synthesis and material characterization

$TiNb_2O_7$ was prepared by both, high-temperature solid-state reaction at 1350 °C for 40 h in air using stoichiometric amounts of TiO_2 (Chempur, 99.9 %) and Nb_2O_5 (Alfa Aesar, 99.9985 %), and by a sol-gel synthesis route from stoichiometric amounts of dried titanium(IV) isopropoxide (Acros Organics, >98 %), and niobium chloride $NbCl_5$ (Alfa Aesar, > 99.9 %), which were stirred in dry isopropanol at room temperature. After complete evaporation of the solvent, the resulting gel was dried at 80 °C and calcined for two hours at 800 °C.

For phase analysis, powder X-ray diffraction measurements were carried out using a STOE STADI P diffractometer with Co-$K_{\alpha 1}$ radiation (λ = 1.78896 Å) in a transmission mode, while scanning electron microscopy (SEM) was applied for characterization of particle morphologies. Therefore, a ZEISS Leo Gemini 1530 microscope was used with an inlens detector at an acceleration voltage of 15 kV. The diffraction patterns are presented in Fig. 2 together with SEM micrographs. Both TNO materials adopt the *C*2/*m* space group, with the lattice parameters *a* = 20.4576(3) Å, *b* = 3.81624(5) Å, *c* = 11.9429(2) Å, β = 120.212(1)° for TNO after the solid-state synthesis, and *a* = 20.487(2) Å, *b* = 3.8112(3) Å, *c* = 11.966(1) Å, β = 119.851(5)° for TNO after the sol-gel synthesis. As known for nanoscale materials, broadening of Bragg reflections and a lower signal-to noise ratio are their characteristic features. Moreover, shape of nanoparticles and a preferred orientation effect considerably change the XRD data, decreasing intensities of some groups of reflections.[20] Additionally, a slight shift of Bragg reflections in comparison to microscale materials towards lower diffraction angles indicates a tensile strain in crystallites, arising from crystal defects.[21]

The solid-state reaction provides particles without any specific shape of several micrometers in diameter, while the sol-gel synthesis results in round particles of nearly 250 nm in diameter.

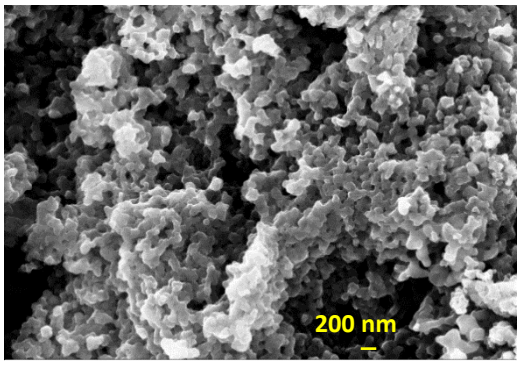

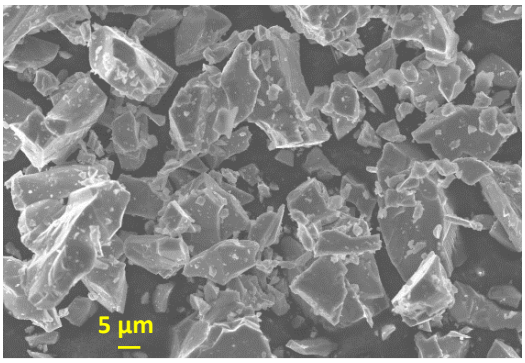

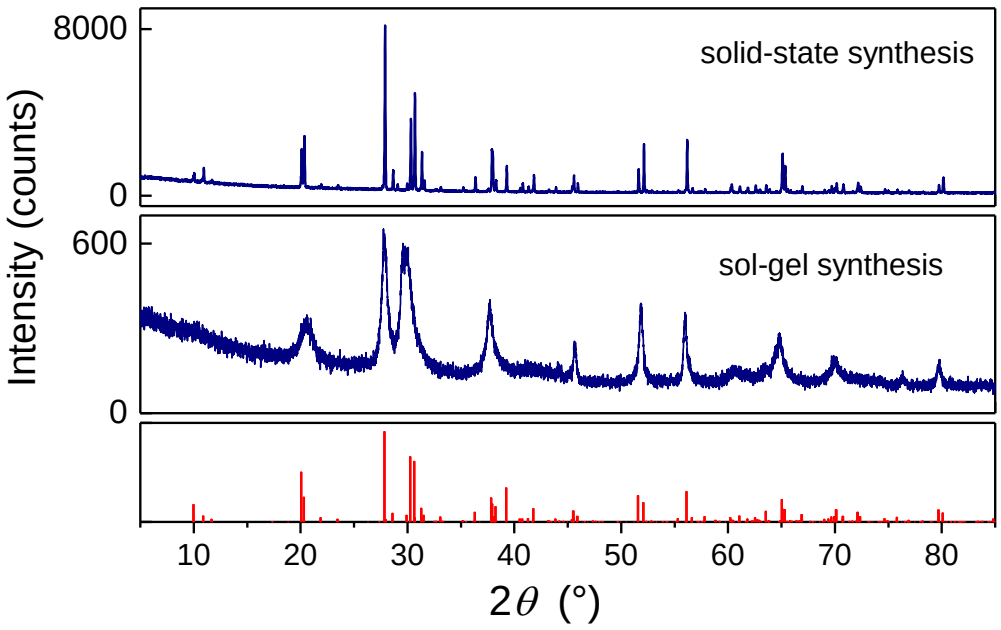

Figure 2. SEM micrographs of $TiNb_2O_7$ after sol-gel (left) and solid-state (right) synthesis, and corresponding diffraction patterns with a theoretical diffraction pattern (Space group *C*2/*m*, ICSD 048109).

For determination of a specific surface area and pore size distribution of TNO after the sol-gel and solid-state synthesis, nitrogen sorption experiments were carried out using a Quadrasorb SI (Quantachrome Instruments) at 77 K. The measurements were performed after outgassing the samples (about 40 mg) in dynamic vacuum at 120 °C for 20 h in a FloVac Degaser, see Fig. S1. The specific surface area calculated at a relative pressure $p/p_0 = 0.1 – 0.3$ using the multipoint Brunauer-Emmett-Teller (BET) method,[22,23] was 9.033(2) $m^2\ g^{-1}$ for nanoscale TNO (sol-gel synthesis), while 5.448(2) $m^2\ g^{-1}$ for the microscale TNO (solid-state synthesis). The pore size distribution was obtained using the Quenched Solid Density Functional Theory (QSDFT) for slit and cylindric pores,[24,25] and the total pore volume was calculated at a relative pressure $p/p_0 = 0.9$. The total pore volume was estimated as 0.0124(4) $cm^3\ g^{-1}$ for nanoscale TNO, and as 0.0086(4) $cm^3\ g^{-1}$ for the microscale TNO. The microscale material shows only nano-pores of 5-7 nm, incorporated into micrometer-sized particles, while the nano-material demonstrates pores of mostly two sizes, with 3 nm, and between 13 and 30 nm. The latter pores seem to be placed within agglomerates which are composed of nanoparticles.

Electrochemical studies

Electrochemical tests were performed in two-electrode Swagelok-type cells using a VMP3 potentiostat (BioLogic). For *operando* experiments and electrolyte composition tests, electrodes were prepared by pressing a mixture of the microscale active material with Super P carbon (BASF) and PTFE (Aldrich) in an 80:10:10 weight ratio onto a stainless steel or copper current collector. For galvanostatic tests at high rates, electrodes were prepared *via* a doctor blade technique using a coating set (Coat master 510, Erichsen and film applicator Zehntner ZUA 2000) from the slurry containing the nanoscale TNO material, Super P carbon and PVDF binder (Solef 1013, Solvay), with the weight ratio 80:10:10, and N-Methyl-2-pyrrolidon (NMP) as a solvent. The electrodes were dried at 80 °C overnight, the loading was about 2.5 mg cm^{-2}.

Magnesium and lithium chips (99.9 %, G-Materials) were carefully polished and used as anodes. A glass fiber cloth (Whatman, GF/D), soaked with electrolyte, served as separator. All Phenyl Complex (APC) electrolytes were prepared by reaction of stoichiometric amounts of $AlCl_3$ (99.985 %, Alfa Aesar) and Phenylmagnesium chloride (Sigma Aldrich) in THF (≥ 99.9 %, Sigma Aldrich). LiCl (99.9 %, Alfa Aesar) in various concentrations was added to these solutions as a lithium source. Galvanostatic Cycling with Potential Limitation (GCPL) was carried out in various potential windows using multiple C-rates, where 1C denotes the current necessary to insert 1 Li per formula unit within one hour, corresponding to 77.5 mA g^{-1}.

Transmission electron microscopy studies

Post mortem TEM studies were carried out in a FEI Titan 300-80 Microscope with third-order spherical aberration correction. Microscale and nanoscale TNO materials were tested after the first discharge and after a prolonged cycling, in the discharged state as well. The samples were loaded by onto Cu 300 mesh TEM grids (Agar) and holey carbon film on Cu 300 mesh TEM grids (Plano) under very short exposure in air of several seconds. High-resolution imaging and diffraction pattern analysis were performed at 300 kV.

Operando synchrotron studies

X-ray powder diffraction

Operando X-ray synchrotron diffraction measurements were conducted at PETRA III, beamline P02.1 (DESY, Hamburg, Germany) and at the MSPD beamline at ALBA Synchrotron (Barcelona, Spain). An eight-fold coin cell holder, connected to a BioLogic Instruments potentiostat, was applied as described previously.[26]

A wavelength of 0.20718(1) Å was determined for experiments at PETRA III and 0.41311(1) Å for experiments at ALBA by a refinement from the reflections of the LaB_6 reference material. For characterization of pristine materials, the first diffraction pattern was recorded before starting the electrochemical measurement. Subsequently, the cells were discharged and charged at a constant current. All diffraction patterns were analyzed by the Rietveld or Le Bail method using Fullprof.[27] Bragg-reflections of the Cu current collector served as an internal standard during the measurements since the refined unit cell metrics of Cu provided an independent control of the reliability of the obtained structural model parameters for the studied materials. A phase-related shift was included into the refinement.

X-ray absorption spectroscopy

Operando and *ex situ* X-ray absorption experiments were carried out on macroscale TNO materials at the beamline P65 at PETRA III extension (DESY, Hamburg, Germany) in transmission and fluorescence setup. As described for the *operando* XRD measurements, a coin cell holder, coupled with a Biologic Instruments potentiostat, was used for electrochemical cycling.

DFT calculations

Structural optimizations have been performed using the projector-augmented wave code VASP version 5.4.4[28,29] with the default pseudopotentials.[30] Total energies have been calculated using the full potential code fplo version 18.00-52[31] within the generalized gradient approximation (GGA).[32] Alternatively, we calculate the GGA+*U* *t*otal energies using an additional on-site Coulomb repulsion *U*

of 2eV within the Ti *3d* and Nb *5d* shells. The around-mean-field scheme has been employed for the double counting correction. The *k*-mesh used for $Li_xTiNb_2O_7$ series ($MgTiNb_2O_7$) comprises 288 (252) points in the irreducible wedge. The larger unit cells for $Mg_xTiNb_2O_7$ ($0 < x < 1$) are sampled with sparser meshes of 75 to 180 points in the irreducible wedge.

RESULTS AND DISCUSSION

As already shown using structure visualization, the TNO lattice could be potentially accessible for both, Li- and Mg-ions, from the geometrical point of view. Moreover, partial intercalation of one type of cations (Li or Mg) can facilitate the intercalation of the other cation type. To examine this hypothesis, energies of Li- and Mg-intercalated phases were calculated and compared with among each other at different states of intercalation.

1. Computational stability analysis of Li- and Mg-intercalated TNO structures

The crystal structure of $TiNb_2O_7$[33] features a strong Ti/Nb antisite disorder, making DFT analysis very challenging. In principle, any ordered configuration satisfying the Ti:Nb=1:2 stoichiometry is possible. But even if we restrict ourselves to the smallest cell accommodating 6 Ti and 12 Nb atoms, the sheer number of possible configurations (18! / 12! / (18-12)! = 18564) is too big for a straightforward analysis. To keep the problem computationally feasible, we consider a simplified structure with a largely lifted Ti/Nb disorder. This model is compatible with 36 Ti-Nb-ordered configurations, and only seven thereof are inequivalent. For these seven configurations, we calculated the GGA energies using VASP on a 4x4x4 k-mesh. Since the energy difference between the two configurations with lowest energies is sufficiently large (~0.1 eV per cell), the ordering of Ti/Nb corresponding to the lowest energy was used for all further DFT calculations.

Experimental information on the crystal structures of the related intercalated compounds is scarce. Catti *et al*.[34] studied the crystal structure of $Li_{2.67}TiNb_2O_7$ using neutron powder diffraction. However, the sizable displacement parameters for Li atoms hint at inaccuracies in the respective coordinates. To the best of our knowledge, crystal structures of Mg-intercalated phases have not been reported.

In the calculations, we adopted the unit cell parameters for $TiNb_2O_7$ and $Li_{2.67}TiNb_2O_7$ from Gasperin[33] and Catti *et al*.[34], respectively, and used a linear interpolation for all intermediate Li compositions. For the unit cell parameters of a hypothetical $Mg_xTiNb_2O_7$ compound, we used the respective parameters of $Li_{2x}TiNb_2O_7$. Having fixed the lattice parameters in this way, we performed GGA calculations to optimize all internal atomic coordinates until all forces are below 0.01 eV/Å. For $LiTiNb_2O_7$ and $Li_{2.67}TiNb_2O_7$, Li atoms were manually placed into the cavities of the crystal structure. The optimized Li coordinates are as the initial guess for $Li_{0.33}TiNb_2O_7$ and $Li_2TiNb_2O_7$, respectively, where all possible configurations with one Li site taken out are relaxed, and the one with the lowest energy was further used for total energy calculations.

As we discussed before, both Li and Mg ions may be intercalated into the structure of $TiNb_2O_7$. This process is governed by energetic and kinetic contributions. While the latter are generally difficult to assess, we can estimate the energetic contributions using density functional theory (DFT) calculations. In particular, we address two relevant questions: Is the intercalation of Li energetically favorable compared to Mg? And how is the cell voltage affected by the intercalation of Li or Mg?

To answer these questions, we constructed $Li_xTiNb_2O_7$ and $Mg_xTiNb_2O_7$ unit cells corresponding to various *x* stoichiometries (up to 2.67 for Li and up to 1 for Mg) and calculated their total energies within the generalized gradient approximation (GGA) and GGA+*U*. The details of our computational approach are described in the Methods section.

The energetic cost ΔE of a Mg intercalation with respect to a Li intercalation can be estimated as

$$\Delta E = E(Li_xTiNb_2O_7) + 1/2 \cdot x \cdot E(Mg) - E(Mg_{x/2}TiNb_2O_7) - x \cdot E(Li), \quad (1)$$

where the energies are in eV per formula unit (*f. u.*). The dependence of ΔE on x is shown in Figure 3 (left). Note that ΔE remains negative in the entire x range, i.e. Li intercalation is energetically more favorable. This also implies that any observed Mg intercalation is kinetically driven. Moreover, the energy cost grows with x, and hence Mg intercalation is possible only for small x values in presence of Li.

Next, we address electrochemical processes. Neglecting the entropic contributions to the Gibbs energy, the voltage (in V) can be estimated from the Nernst equation:[35]

$$\Delta V = V_{x1} - V_{x2} = - [E(Li_{x1}TiNb_2O_7) - E(Li_{x2}TiNb_2O_7) - (x_1 - x_2) \cdot E(Li)] / (x_1 - x_2) / F \quad (2)$$

where the total energies are in eV per f. u., F is the Faraday constant and $x_1 > x_2$. To calculate the voltage in the case of a Mg intercalation, the denominator is doubled due to the twice larger number of electrons. The resulting voltage curves are shown in Figure 3(left). There is only a small difference between GGA and GGA+U, which will likely increase for larger U values. The process of Li intercalation agrees well the experiment: discharging starts from a rather high voltage of 2.4 V and then drops to 1.5 V while remaining nearly constant up to x=2.

Therefore, intercalation of both Li and Mg cations into TNO is favorable from the enthalpy point of view. Moreover, a significant entropy increasing upon Li-intercalation concluded in Catti *et al.*[34], additionally acts as a driving force for Lithiation. Similar effect can be expected for Mg-intercalation. Being both presented in the electrolyte, Li cations are, however, preferable for insertion into TNO over Mg cations.

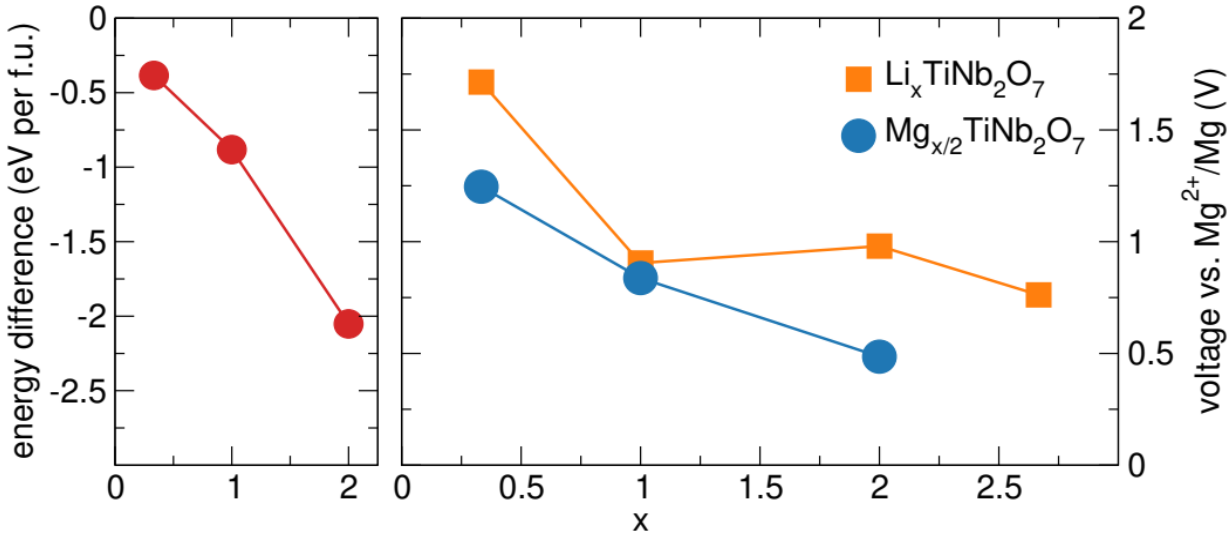

Figure 3. Left: energy difference (eV per *f.u.*) between the intercalation of x Li atoms with the corresponding intercalation of x/2 Mg atoms, as calculated using Eq. (1). Li intercalation is energetically favorable for any x. Right: The voltage curves for appropriate cation insertion of x Li or x/2 Mg into TNO, giving $Li_xTiNb_2O_7$ and $Mg_xTiNb_2O_7$ calculated using Eq. (2), and plotted *vs*. the Mg^{2+}/Mg redox pair.

2. Studies on charge storage mechanism in microscale TNO during operation in a Mg-Li battery

As already shown in the literature,[12] during discharge of a Li-cell with a TNO electrode (current density of 48 mA g^{-1}), both Ti and Nb are reduced, while the lattice parameter *b* and unit cell volume increase quasi-linearly with the Li-content in the material. Although theoretical calculations favor a pure Li-insertion into TNO in presence of Mg cations in hybrid Mg-Li batteries, a co-intercalation of both kind of cations may still be possible because of kinetic reasons. Further, we elaborate the reaction mechanism in TNO during operation in a Mg-Li hybrid battery at a low near-open-circuit-voltage (OCV) experimental current density of 12 mA g^{-1}.

2.1. Exploration of metal valence changes in TNO in Mg-Li batteries

To study the change in the valence state of both metals as a function of the cell potential, the Nb-*K* edge spectra of TNO were measured under *operando* conditions during the cell discharge and charge, while Ti-*K* edge spectra were recorded *ex situ* for the initial, discharged and charged states.

It is well-known that the position of the absorption edge E_0 in 3d and 4d transition metal oxides correlates with the metal valence state.[36] The absorption edge E_0 can be defined using various approaches: either as the energy corresponding to the maximum of the energy derivative of $\mu(E)$, which is in coincidence with the inflection point of the absorption edge,[37] or as the energy at the x-ray absorption coefficient $\mu(E)$ = 0.8 of normalized post-edge intensities,[38] that often provide the same adsorption edge energy.

The energy positions at $\mu(E)$ = 0.8 of Nb-K and Ti-K edges fits perfectly with Nb_2O_5 and TiO_2 reference materials, pointing at the presence of Nb^{5+} and Ti^{4+} in TNO. During Mg-Li cell charge, the Nb-*K* edge shifts permanently to smaller energies, confirming a constant redox process between Nb^{5+} and Nb^{4+}. The Ti-*K* spectra in Figure 4 demonstrate that the pristine and the charged oxide coincide with the TiO_2 reference, while the discharged sample exhibits an edge shift towards lower energies, resulting in partial reduction of Ti^{4+} to Ti^{3+}. The change in the Nb-K edge of more than 1.5 eV and of about 1.0 eV in the Ti-K edge at $\mu(E)$ = 0.8, measured for the x-value in $(Li,1/2Mg)_xTiNb_2O_7$ of 1.5, is in agreement with values reported in previous works[12,39] for TNO being cycled in Li-batteries.

Since XAS is a bulk-sensitive technique, these results clearly indicate the presence of bulk redox processes in TNO in Mg-Li cells. If the storage mechanism would be dominated by redox pseudocapacitance, then such a clear gradual redox of all involved metals could not be observed. Therefore, the capacitive contributions, obtained from sweep-dependent CV in both, Mg-Li and Li-cells on microscale TNO in previous work,[19] must be clearly considered as an intercalation pseudocapacitance, according to the definition of Augustyn *et al*.[40]

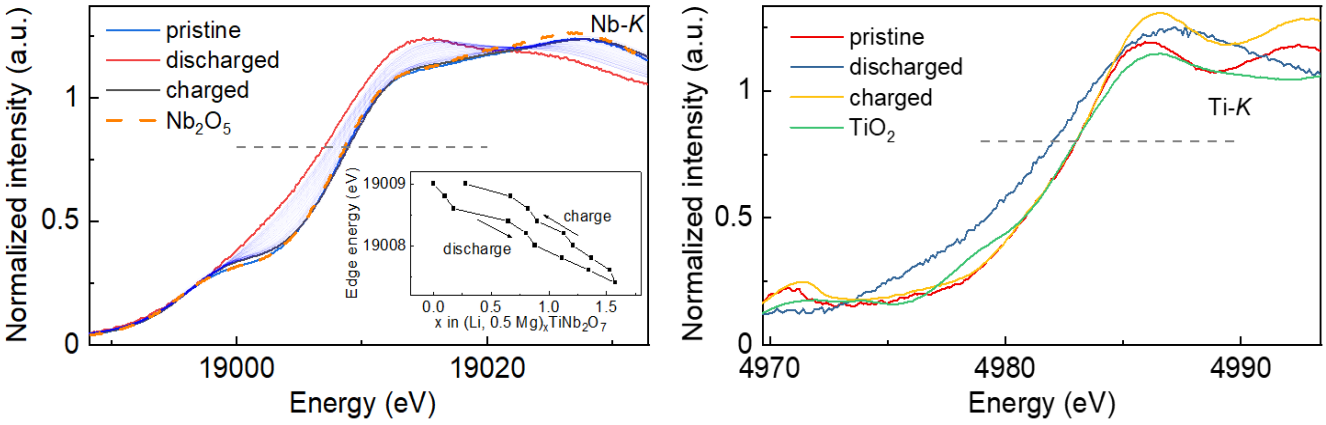

Figure 4. X-Ray absorption spectra of macroscale TNO recorded *operando* in a Mg-Li cell with 0.1C at the Nb-*K* edge, and measured *ex situ* at the Ti-*K* edge, after operation in a Mg-Li cell.

2.2. Evaluation of structural changes in TNO in Mg-Li batteries

Analysis of the structural changes in TNO during operation in Mg-Li batteries and their comparison with the structural behavior in Li-batteries can provide information regarding a possible Li,Mg-co-intercalation into the TNO electrode. Hence, we explored the evolution of the crystal structure during discharge and charge of microscale TNO in Li- and Mg-Li cells using a slow rate of 0.1C, see Fig. 5a. Note, the capacity of *in situ* Mg-Li cell is usually lower than obtained in Swagelok-cells at the same current density, which is probably due to a low compatibility between *in situ* cell components and the dual-salt electrolyte. A comparison of the TNO diffraction patterns of the Li- and Mg-Li cells at the same state of discharge, which was calculated from the amount of current flowing through the cell during the galvanostatic experiment, clearly points at differences in cell metrics of TNO, since the positions of Bragg reflections are shifted to both, smaller and larger 2θ values, and their intensities are different, see Fig. 5b.

In the literature, a detailed structural analysis of Li-intercalated TNO including cation and anion sites, interatomic distances and occupancies of possible Li-positions is reported solely for two compositions $Li_{2.67}TiNb_2O_7$ and $Li_{3.33}TiNb_2O_7$, using *ex situ* neutron powder diffraction studies and first-principles calculations.[34] Other structural investigations were performed *operando* or *ex situ* using laboratory or synchrotron XRD experiments. Based on the shape of the electrochemical curve in galvanostatic experiments, it has been generally assumed in the literature that lithiation occurs as a solid-solution process between $0 \leq x(Li) \leq 0.88$ in $Li_xTiNb_2O_7$ (slope in the curve), followed by a two-phase mechanism for $0.88 \leq x(Li) \leq 2.67$, corresponding to a plateau in the curve, and finally again by a solid-solution mechanism for $x(Li) > 2.67$ (slope in the curve).[12,39,41] Although lattice parameters for the initial and Li-containing TNO were reported several times, the structural information regarding the second phase is completely missing in these works. All studies confirm a nearly linear dependence of the lattice parameter *b* and the unit cell volume on the amount of intercalated Lithium.[12,34,39,41] In contrast, the dependence of the *a*- and *c*-parameters on the lithium amount is less obvious, although the *a*-parameter shows a maxima-like behavior at the beginning of insertion.[12]

We performed a Le Bail-based analysis of the TNO structural data recorded during discharging, in both Li- and Mg-Li cells. In the last case, a Mg-co-insertion cannot be unambiguously ruled out. The evolution

of TNO lattice parameters in the Li-battery is very complex, especially in the range of the intercalated Li-amounts x(Li) between 0.8 and 1. A very similar structural behavior of TNO in Li-batteries has been reported,[12] although both materials exhibit quite different morphologies (60-80 nm particles in the previous work[12] *vs*. microscale particles in present work) and most probably different Ti/Nb ratio in sharing cation sizes in the TNO structure because of different synthesis temperatures (700 °C in the work[12] *vs*. 1350 °C in present work). The behavior upon lithiation was assigned to a solid-solution process, followed by a two-phase coexistence region with the second phase being isostructural to pristine TNO. However, the incorporation of the second TNO phase into the structural model was necessary at x(Li) ≈ 2, corresponding already to the midpoint of the electrochemical plateau. Here we would like to make a note of caution. For low-symmetrical systems with a big unit cell, the formation of a second phase and strong structural strains both result in a broadening of Bragg reflections. To distinguish between these two issues in such complex systems is rather challenging, because both phenomena result in a significant peak broadening, thus needing to be studied in detail separately.

However, a comparison between cell metrics for both Li- and hybrid Mg-Li batteries at the same discharging state, shown in Figure 5c, reveals large differences. Clearly, we observe a less severe change of lattice parameters and volume in the hybrid Mg-Li battery than in the Li battery when comparing the same degree of the cation insertion. The difference in cell metrics between TNO in Li- and Mg-Li batteries sets after about x(Li) ≈ 0.15, although the character of changes (maximum in the *a*- and *c*-parameters and a nearly linear increase in the *b*-parameter) remains. Moreover, in the Mg-Li battery, the introduction of a second isostructural phase into the structural model is already necessary at x=1.25, where x denotes 1 Li or 0.5 Mg. Hence, two possible scenarios can be considered in order to explain the discrepancy in TNO cell metrics during operating in Li- and Mg-Li batteries: *i*) a co-intercalation of some Mg-amount into TNO from the dual-salt electrolyte in the Mg-Li battery, *ii*) various Li-migration paths and Li-location on other crystallographic sites in the TNO structure in the Mg-Li dual electrolyte. Of course, both of the scenarios can also take place simultaneously.

Whereas the first scenario could easily be proven using spectroscopic methods, the second one is non-trivial. In the $Li_{3.33}TiNb_2O_7$ composition, there are 5 partially occupied Li-sites per unit cell, which exhibit different energies.[34] According to the first-principle calculations, performed for compositions $Li_xTiNb_2O_7$ ($1 \leq x \leq 4$) with Li-atoms successively occupying free Li-positions Li1-Li4,[36] the lattice parameters change non-linearly with increasing Li-content. This non-linear behavior was later confirmed experimentally at least twice,[12,41] although the published absolute values of cell parameters at the same Li-content differ in both publications. It is feasible that different particle morphology and different Ti/Nb distributions over the cation positions in the crystal structure facilitate Li-penetration from the electrolyte into the solids through certain crystallographic surfaces, enabling Li-movement along other diffusion pathways, and occupation of alternative sites by Li-cations.

A more complex electrolyte composition in the case of Mg-Li hybrid batteries with a variety of Li- and Mg-species can additionally influence diffusivity of Li and Mg cations through the cathode electrolyte interface. As theoretical studies on complex electrolyte systems showed, diffusion phenomena in such multiple electrolyte systems cannot be considered independently for each cation type.[42]

The EDS analysis of microscale TNO after first discharge in a hybrid Mg-Li battery with 7.75 mA g^{-1} yielded 22-25% Mg in the material, calculated as an average value for several test areas, thus confirming a co-insertion of Mg and Li (Figure S2a-d). Nearly the same amount of Mg was detected in the material after a long-term cycling, pointing to a reproducible intercalation behavior. After cycling

of the nanoscale TNO at 1160 mA g^{-1}, still more than 10% Mg was detected. All materials remain crystalline after prolonged cycling, independently on the current density.

To conclude, a partial co-insertion of Mg into TNO occurs starting from the composition $Li_{0.2}TiNb_2O_7$, if the current density is low enough. Obviously, some initial Li-insertion is necessary to expand the crystal structure to some extent, facilitating Mg^{2+} penetration. Such a pre-lithiation mechanism with following Mg-insertion is already known for oxides.[43]

Moreover, the smaller ionic radius of Mg^{2+} with 0.72 Å in comparison to Li^+ with 0.76 Å for an octahedral oxygen surrounding[8] and a double charge contribute to a lattice contraction. However, neutron powder diffraction experiments on the intercalated material are further necessary for a comprehensive structural characterization.

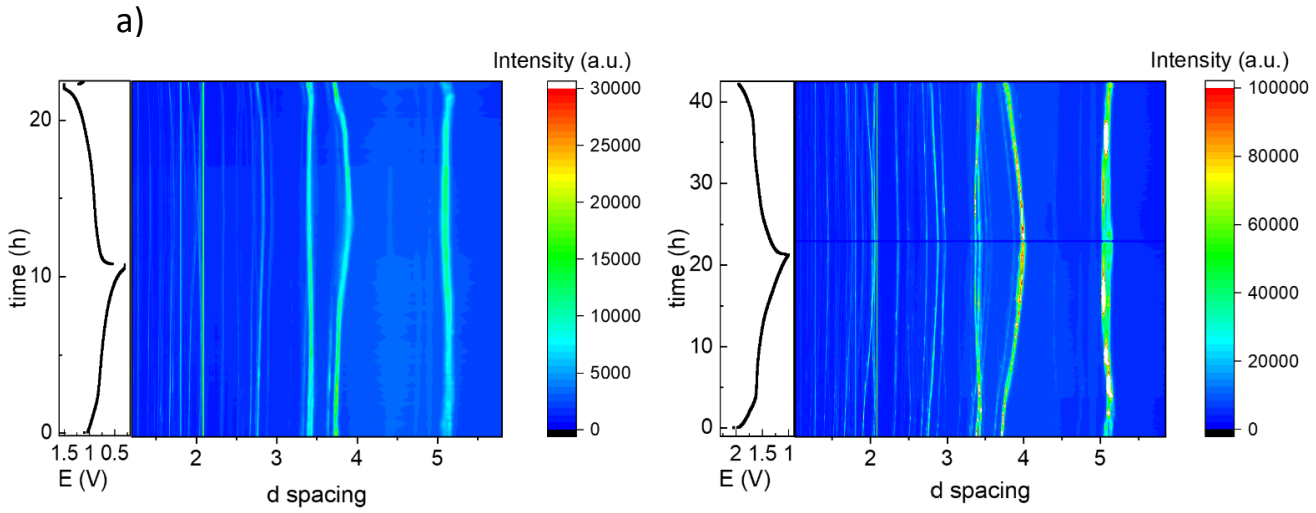

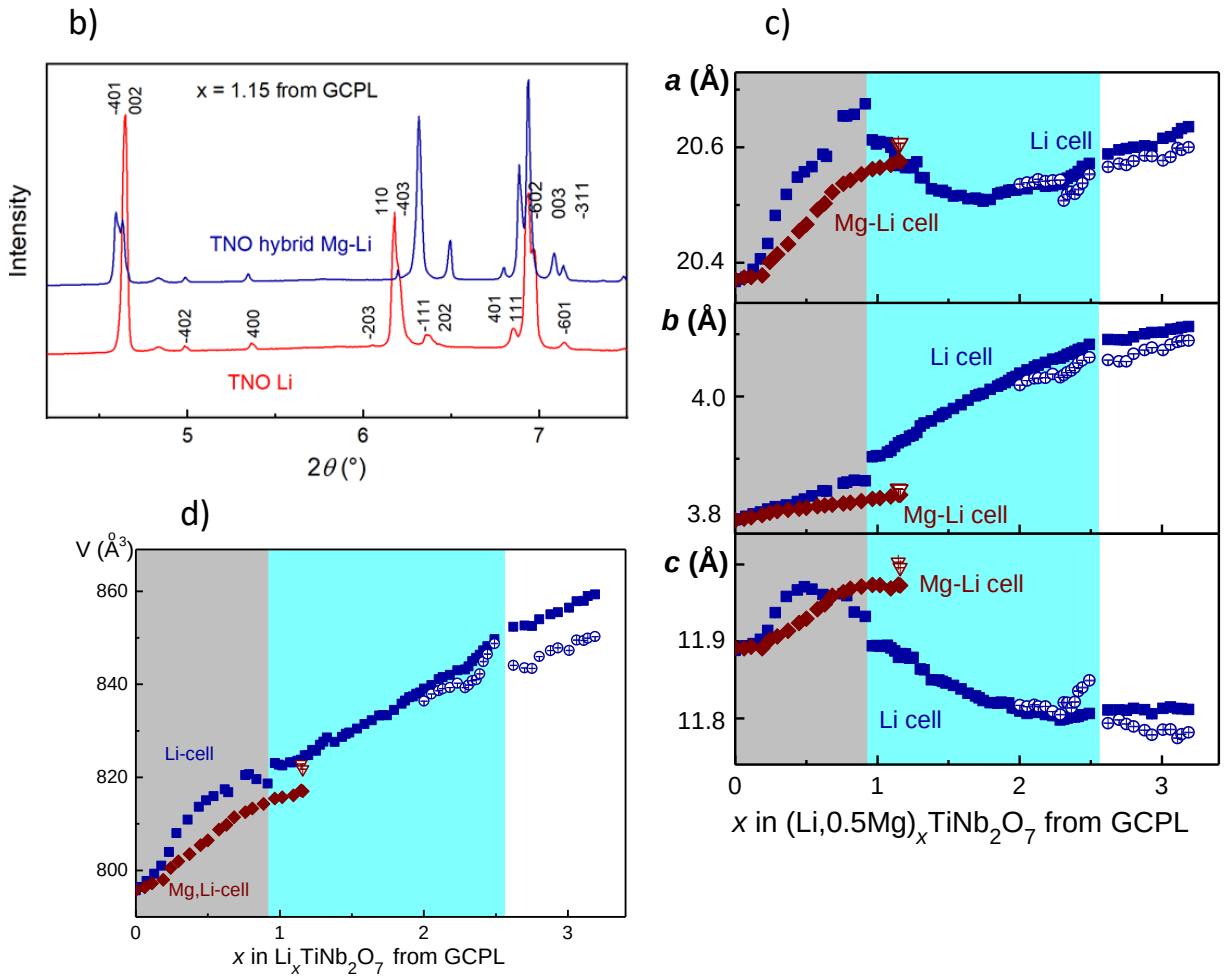

Figure 5. a) Contour plots of synchrotron diffraction patterns recorded by operando measurements of a Li- (right) and a hybrid Mg-Li (left) cell with macroscale TNO, cycled at 7.75 mA g^{-1}, b) comparison of diffraction patterns of TNO in a hybrid Mg-Li battery and a pure Li battery at similar electrochemical intercalation states, c)-d) corresponding unit cell volumes, obtained from Rietveld analysis. Full symbols represent the initial phase, while hollow ones indicate the appearing phases. Note that error bars are inside the scatters due to the good quality of the obtained data.

3. Electrochemical studies

3.1. Effects of the electrolyte composition

According to our DFT calculations, lithiation of $TiNb_2O_7$ is preferable over Mg-insertion in a dual-salt Mg,Li-electrolyte, whereas structural studies as well as EDS pointed about 20% Mg-co-intercalation at a very low current density. Since the Li-diffusion in solids is generally expected to be orders of magnitude faster than the Mg-diffusion,[44] the amount of Li inserted into $TiNb_2O_7$ must be directly proportional to the Li-concentration in the electrolyte at low concentrations. Moreover, although the concentration of Li^+ cations and, therefore, their activity in the electrolyte will decrease during discharge, the lithiation process nevertheless cannot be completely switched to magnetization. This is due to the fact that the difference between energies of hypothetical $Li_xTiNb_2O_7$ and $Mg_{x/2}TiNb_2O_7$ phase becomes even larger with the pronounced intercalation.

First, we tested electrochemical Mg^{2+} insertion into microscale TNO in a Li-free 0.4M APC electrolyte, see Figure 6(left). Evidently, negligible Mg insertion into TNO from a pure APC electrolyte occurred in the Mg-battery, whereas in case of the APC + LiCl electrolyte with different LiCl concentrations, TNO delivers an electrochemical response (Fig. 6(right)). This allows to conclude that the presence of Li^+ is necessary to enable the redox process. Note that measurements with a Mg-free LiCl/THF electrolyte and a metallic Li anode as a reference battery showed a very unstable behavior. Further electrochemical insights are provided by cycling of TNO electrodes in APC + LiCl electrolytes with varying Mg and Li concentrations, as depicted in Figure 6(right). In all tests, the total amount of Li and Mg from the electrolyte was enough to form a hypothetical $A_3TiNb_2O_7$ phase with *A* - Li, Mg, see Table S1. Generally, a higher concentration of APC in the electrolytes leads to higher capacities. The role of the LiCl quantity at a fixed APC concentration for the resulted capacities is more complex. In the 0.2M APC electrolyte, a capacity limitation was observed with increased LiCl amount starting from 0.6M LiCl. In the 0.4M APC electrolyte, the capacity still increased with the LiCl amount, although the 1.25M LiCl solution corresponds to the highest LiCl amount which could be dissolved in 0.4M APC. Further detailed studies of electrolyte compositions would be advisable in order to understand the cooperative effect of all cations in the electrolyte (Li, Mg, Al) for the electrochemical performance.

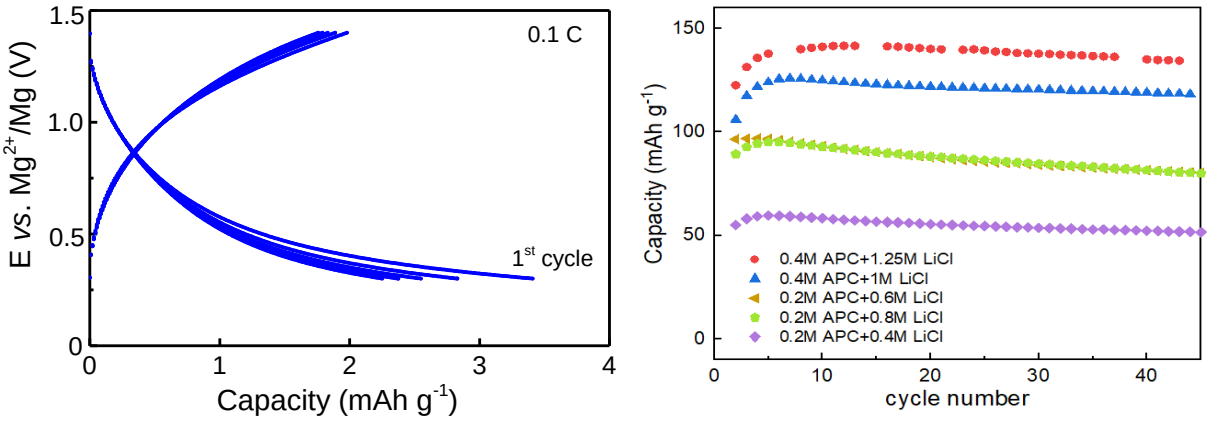

Figure 6. left) The first fife galvanostatic cycles of microscale TNO in a Mg-Battery with 0.4M APC electrolyte at 7.75 mA g^{-1} (0.1C), right) cycling behavior of microscale TNO in dual-salt electrolytes of different ratio APC-LiCl at 1C.

3.2. Cycling behavior

a) Kinetics of TNO in Li- and hybrid Mg-Li batteries

As it has been already mentioned, our previous work on microscale TNO in hybrid Mg-Li batteries revealed a significant capacitive-like contribution of about 53 % at 0.01 mV s^{-1} to the charge storage mechanism in TNO,[19] similar to 50.9 % at 0.05 mV s^{-1} as reported for TNO with a particle size of about 40 nm in Li-batteries.[18] Generally, the capacity of an insertion electrode material always implies contributions from a non-Faradaic double-layer capacitance and a Faradaic pseudocapacitance, which reflects a redox process on the surface or surface-near region of the electrode without any structural changes in the bulk and without any limitations of the solid-state diffusion. Moreover, for some materials, a definition of a Faradaic intercalation capacitance has been introduced,[40,45] which is mostly determined by ionic diffusion in solids, following, however, a capacitive time constant because of their open crystal structure and a rapid bulk ion movement. Since the contribution of a double-layer

capacitance for microscale materials is negligible, only a redox pseudo capacitance and a Faradaic intercalation capacitance can be considered in case of microscale TNO.

Materials with such a high capacitive contribution are generally beneficial for the cycling with high rates and can be utilized in Li-ion capacitors.[45,46] Redox pseudocapacitance and/or intercalation pseudocapacitance provide the main contribution to the capacity.

In order to estimate the diffusion-limited and capacitive contributions to the overall capacity as dependent on the current density in a hybrid Mg-Li battery with TNO, and to compare them with TNO in a Li-battery, galvanostatic charging/discharging experiments at different current densities were carried out. In parallel, we considered a simplified model of the Li-intercalation into a spherical particle, assuming that the cation diffusion as a time-limited process. Based on Fick's second law, a cation diffusion length *L* along one direction in solids can be roughly estimated from the diffusion coefficient *D* and the diffusion time *t* at a constant temperature using the equation $L = 2\sqrt{D\,t}$.[47] Taking into consideration the previously measured average diffusion coefficient of $1*10^{-14}$ cm^2 s^{-1} for the microscale TNO in hybrid Mg-Li and Li-batteries using galvanostatic intermittent titration (GITT),[20] and the average diameter of particles of 250 nm with nearly a spherical shape (as determined from SEM studies), a diffusion length as a function of time was calculated (Fig. 7a). On the other hand, the diffusion length is directly proportional to the capacity in a diffusion-limited process, meaning that zero diffusion length corresponds to zero capacity while the diffusion length of 250 nm relates to 100 % capacity. The maximum capacities for Mg-Li (240 mAh g^{-1}) and Li-batteries (260 mAh g^{-1}), supposed further for 100%, were defined as values obtained during the second discharge of the battery at a very low rate of 0.1C (7.75 mA g^{-1}).

Thus, in Figure 7a, we can follow the dependence of the measured capacity on the reaction time, which is determined by the applied current. Both Li- and hybrid Mg-Li batteries demonstrated a similar behavior, showing a fast capacity rise at reaction times below 100 minutes and a quasi-saturated behavior in capacities at a higher reaction time, thus confirming similar intercalation mechanisms. The evolution of both curves with the time differs completely from the pure diffusion regime. In general, much higher capacities than calculated from the diffusion-limited model, were detected for the reaction time up to 400 min, in accordance with the previously measured capacitive contributions.

Similarly, two regimes of Li-intercalation into nanoscale TNO were observed during cyclic voltammetry (CV) experiments in dependence on the voltage scan rate as well:[48] above 10 mV s^{-1}, a fast faradaic pseudocapacitive process occurs, whereas below 10 mV s^{-1}, a diffusion-limited kinetics dominates in the storage mechanism.

Nevertheless, small differences in both Li- and hybrid Mg-Li batteries are observable. Thus, applying the same current density of 155 mA g^{-1} leads in case of the Li-battery to capacities of 95% after 100 min, while in case of the Mg-Li battery, only 90% of possible capacity was reached. This issue reflects slightly slower kinetics in the hybrid Mg-Li battery, which could originate from a co-insertion of Mg-cations into TNO, thus partially blocking further Li-movement. Interestingly, a difference in the capacities of about 40 mAh g^{-1} between the Li- and Mg-Li batteries remains nearly constant up to high current densities up to 1.2 A g^{-1} (Fig. 7b) if the first few cycles were performed with a small current of several mA g^{-1}, which are required for the formation of a protected cathode-electrolyte interface.

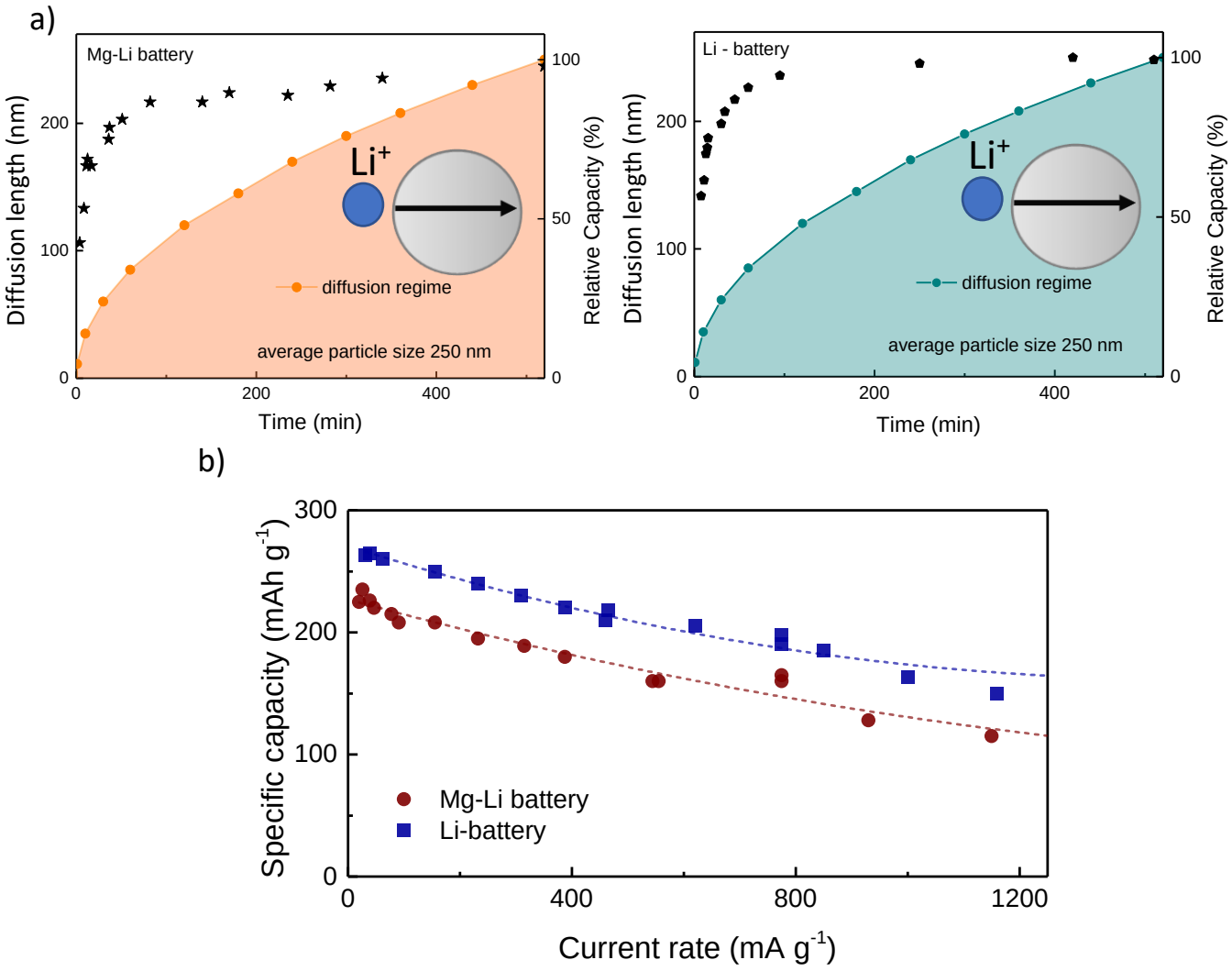

Figure 7. a) Experimental relative discharging capacities of nanoscale TNO as a function of the current density in Mg-Li (asterisks) and Li-batteries (pentagons), together with calculated diffusion length in the assumption of a diffusion regime ($L = 2\sqrt{D\,t}$). Each point represents an average from two measurements. The first measurements were performed at the current density of 1C for both kind of batteries, and then the rate was randomly varied. b) Specific capacity for TNO in Mg-Li and Li-battery in dependence on the current density.

b) Long-term cycling at 25 °C and 60 °C

Long-term cycling behavior of a Mg-Li hybrid battery with nanoscale TNO operated at high rates of 10C and 20C (775 mA g^{-1} and 1550 mA g^{-1}, respectively) was compared with those of a Li-battery; the results at room temperature are depicted in Fig. 8. Note, no formation cycles with a lower rate were performed prior to the main measurements. As a result, for both kind of batteries, a slight increasing of the capacity was observed for the first ten cycles, corresponding to the formation of a cathode-electrolyte-interface (CEI)[19], see Fig. 8a. The cycling stability for both battery types at 10C is very similar for 750 cycles, showing capacity retention of 93% relative to the 10th cycle. Cycling of Mg-Li batteries at 20C results as well in a stable behavior with even a nearly 100% capacity retention, while Li-cells

demonstrate a noticeably unstable cycling and even a collapse before the 1000th cycle. A Mg-Li battery can be operated even over 2000 cycles with capacity retention of 94% (Fig. 8b). The cell polarization, here defined as a difference between charging and discharging curve at the half of capacity, changes with the cycle number differently for both kind of batteries: whereas it becomes lower during the first several cycles and afterward remains constant during hundreds of cycles for the Mg-Li cell, it is still growing with the cycle number for the Li-cell, see Fig. 8c and 8d. Note, especially a discharge curve in the Li-battery shifts to the lower cell potential with the cycle number. We want to add here that this outstanding behavior is obtained with thoroughly blade-coated electrodes on copper foil. Electrodes dry-pressed on a stainless steel mesh exhibited significantly lower capacities at high current densities, see Figure S3.

It has been previously discussed that an impeded lithiation of TNO, due to its strongly insulating nature in the charged (delithiated) state, leads to an asymmetry between charge/discharge processes in terms of capacities.[17] For example, an ultra-fast charging of TNO 1D nanofibers with 7740 mA g^{-1} showed capacities up to 150 mAh g^{-1} at a discharge current of 387 mA g^{-1}. In contrast, if the charge current was set to 387 mA g^{-1}, a discharge capacity reached only 75 mAh g^{-1} at the discharge current density of 7740 mA g^{-1}. An enhanced electronic conductivity of the lithiated TNO in contrast to the lithium-free one was suggested as an origin for observed phenomenon.[18] This phenomenon, however, could not explain the increased discharging polarization of the Li-cell upon cycling, since the polarization of the Mg-Li cell with the same cathode material decreases during battery operation. Therefore, other reasons should be identified to explain a superior performance of the Mg-Li battery.

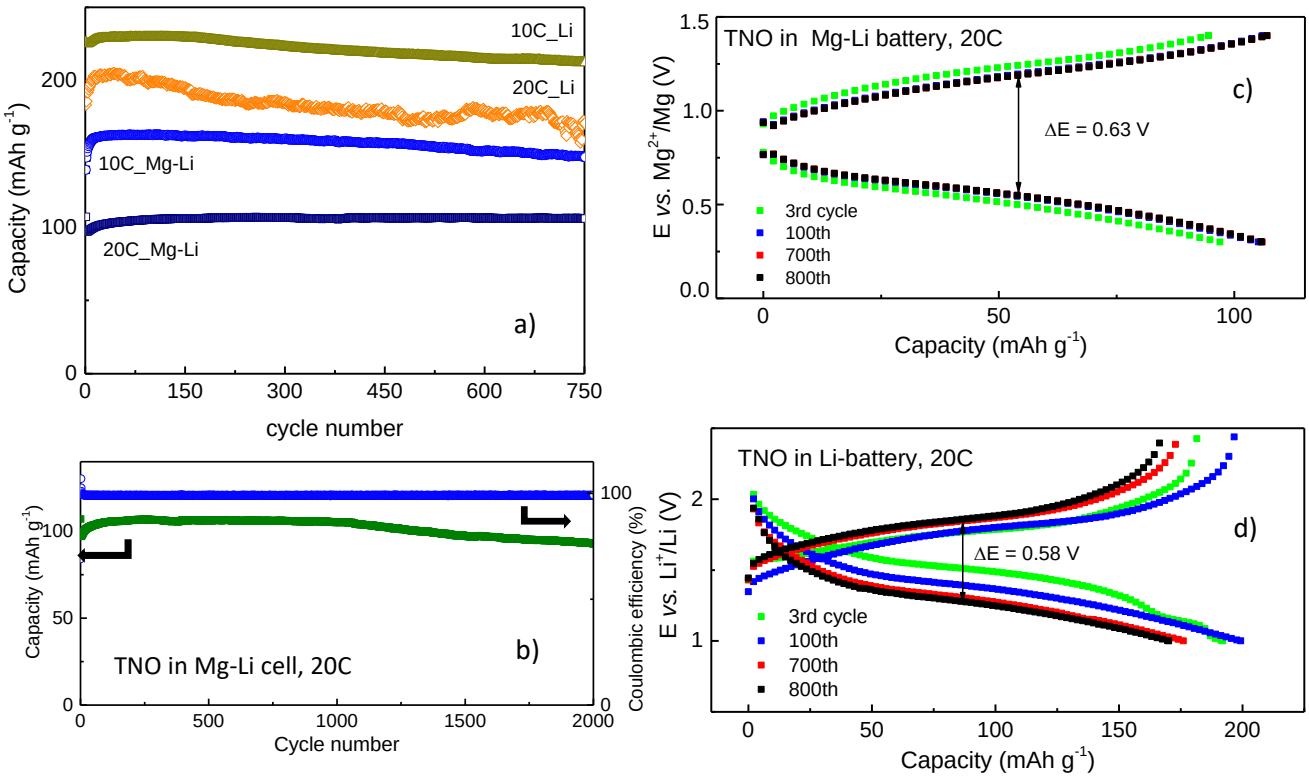

Figure 8. a) Room-temperature cycling behavior of TNO in Li- and hybrid Mg-Li batteries at 10C (775 mA g^{-1}) and 20C (1550 mA g^{-1}). b) Long-term cycling of TNO in a hybrid Mg-Li battery with 20C. c) Typical discharging-charging cycles in Li- and d) hybrid Mg-Li cells.

Operation with the 20C rate at 60 °C revealed more clearly the enhanced cycling stability of the Mg-Li battery in comparison to the Li-battery, see Fig. 9. The capacity of the Li-cell was nearly constant only for the first 15 cycles followed by a strong capacity loss, leading to the capacity retention of 16 % after 500 cycles. This loss is attributed to the instability of the electrolyte and the Li-SEI rather than the TNO electrode. It is known that conventional electrolytes start to decompose above 55 °C[49] while also solid-electrolyte interface formed in solutions of $LiPF_6$ in alkyl carbonates disintegrates at temperatures around 60 °C.[50] On the other hand, the capacity retention of the hybrid Mg-Li cell was still about 86 % after 500 cycles. The Coulombic efficiency (CE) defined here as $Q_{discharge}/Q_{charge}$, was higher than 100 % for both kind of batteries at the beginning of cycling, reflecting the irreversible consumption of charge carriers during battery discharging due to the formation of a cathode-electrolyte interphase (CEI). However, the CEI formation in the Mg-Li battery was completed after the first three or four cycles leading to the CE close to 100 %, whereas the CE in the Li-battery reached 100 % only after 25 discharging/charging cycles and decreased further below 100%, reflecting some side reactions during delithiation of the TNO material.

Analysis of the cell polarization at 60 °C revealed about 0.3 V for the Mg-Li cell in the 1st cycle and 0.35 V in the 500th cycle, whereas 0.24 V in the 1st cycle and 0.7 V in the 500th one was detected for the Li-cell. At this point, it is unclear, whether the increased absolute capacity at higher temperatures is also sustained by a co-intercalation of Mg and Li, as observed at 20 °C. Further *operando* and *post mortem* studies would be necessary to explore this issue.

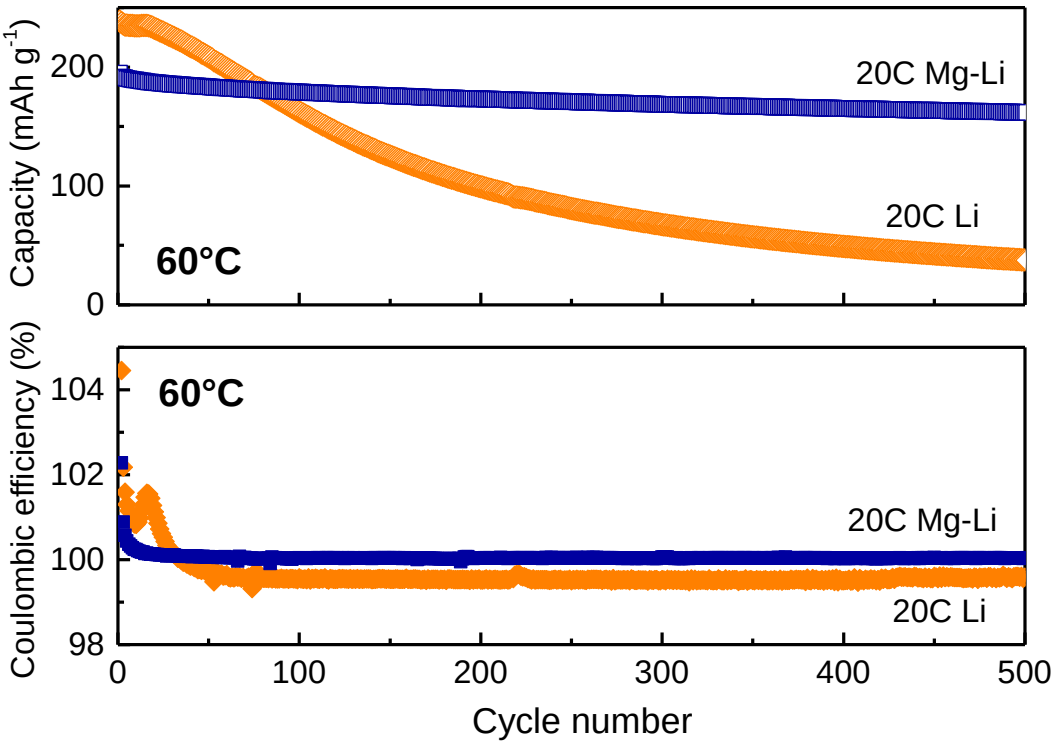

Figure 9. Discharge capacity of TNO in Li- and hybrid Mg-Li batteries at 20C (1550 mA g^{-1}) at 60 °C, together with the Coulombic efficiency, defined as $Q_{discharge}/Q_{charge}$.

c) Comparison of Li- and Mg-anodes at high rates

The reason for the increased performance of the Mg-Li hybrid battery at 20C is found at the anode (Fig. 10). Electrochemical performance of Li- and Mg-electrodes was evaluated in symmetrical cells during repeated galvanostatic stripping/plating using current densities corresponding to 10C and 20C in a hybrid Mg-Li cell (3 mA cm^{-2} and 6 mA cm^{-2}), and charge transfer limitation corresponding to typical capacities in a hybrid Mg-Li cell.

At 10C, Li metal can be cycled with a comparatively low initial overpotential of 0.20 V and a slightly increased value of 0.35 V after 280 h, while Mg in the APC + LiCl electrolyte exhibits a stable overpotential of 0.4 V over 300 h. At 20C however, tremendous increases in the overpotential after 180 h indicate the failure of the Li anode, most probably due to its widely-reported dendrite growth.

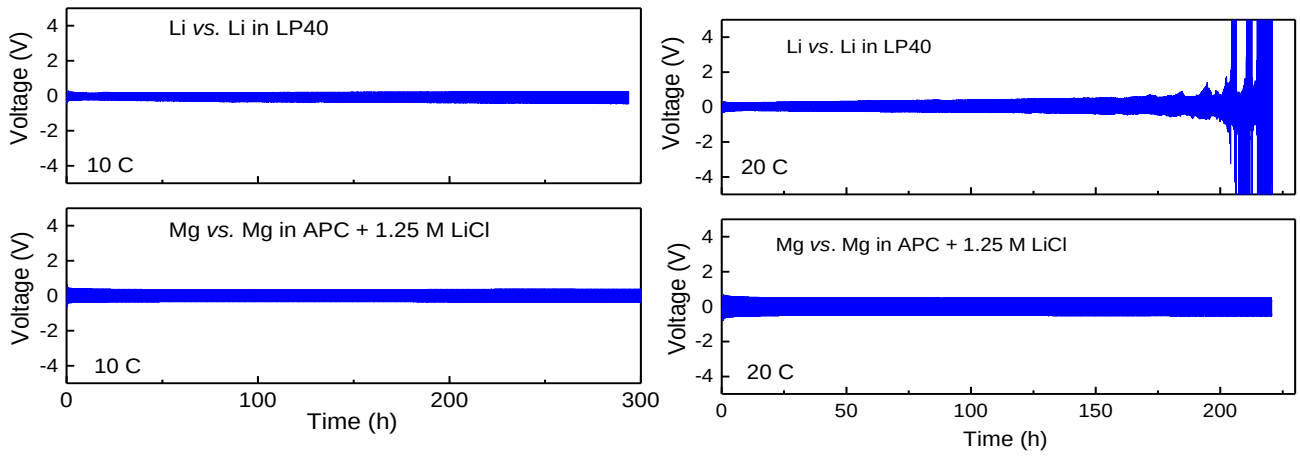

Figure 10. Voltage profiles of the symmetric Li-Li cells with LP40, and Mg-Mg with APC+1.25M LiCl electrolytes cycled with current densities corresponding to 10C and 20C in a typical hybrid Mg-Li cell.

According to Aurbach's early work,[51] the deposition and dissolution of Li leads to a continuous cracking and healing of the surface films, thus increasing the Li surface area and causing dendrite growth. This does not only present a severe safety hazard, as these dendrites can eventually penetrate through the separator. Just as detrimental, a large loss of active lithium is the consequence, since dendritic structures tend to detach from the anode, ending as dead lithium inside the electrolyte.[52] Mg on the other hand maintains a flat cycling profile with a constant overpotential of 0.5 V (Fig. 10). As reported by Matsui[53], Mg deposits from Grignard-based electrolytes do not form dendritic structures which is explained by a strong overpotential dependence, preventing locally concentrated currents, which would favor dendrite growth. In the light of these fundamental studies, our results can be easily understood: although the Mg anode cycles at a higher overpotential, the slightly inhibited deposition is unlikely to result in locally concentrated currents, and a stable cycling is possible. Li however exhibits a lower overpotential, which in turn favors locally concentrated deposition hotspots, leading to dendrite growth and an early anode failure.

DISCUSSION

Hybrid Mg-Li batteries offer certain benefits with regard to safety operation and low costs by keeping many valuable characteristics of Li-batteries, on the one hand. On the other hand, the presence of two

cation types, Li^+ and Mg^{2+} in the whole system complicates understanding the resulting storage processes. Therefore, hybrid batteries should be comprehensively evaluated as a complex system, which includes both positive and negative electrodes, in addition to the electrolyte.

Until now, several classes of intercalation chalcogenides as electrode materials were tested in hybrid Mg-Li batteries operated with an APC electrolyte and a Li-salt, as for example sulfides Mo_6S_8[4] and TiS_2,[7] or oxides VO_2,[54] TiO_2,[5] $Li_4Ti_5O_{12}$,[9] $LiCrTiO_4$,[55] $Li_4Mn_5O_{12}$.[56] For most of them, some enhancements in electrochemical performance in comparison to conventional Li-batteries were reported, although the effects causing the improvement are different.

An improved capacity as an effect of the Li and Mg co-intercalation is a key issue for the Mo_6S_8 cathode in Mg-Li hybrid batteries,[4] since only about 50 % of the capacity usually gained in Li-cells can be obtained in Mg-cells without presence of any Li-cations. Therefore, the insertion mechanism into Mo_6S_8 depends strongly on the Li-concentration in the electrolyte, and an optimal concentration must be found. Mo_6S_8 exhibits a quite stable cycling behavior with superior performance for a Mg-Li battery using an electrolyte with 0.2 M APC and 0.5 M LiCl, showing a 96.4 % of theoretical capacity at 10 C, 93.6 % at 20 C, and 87.5 % at 30 C.[2] This value is significantly higher than 80 mAh g^{-1} for Mo_6S_8 cycled with 1C in a Li-cell with 1 M $LiPF_6$ dissolved in carbonate-based solvents. The reason for the observed difference was not discussed, but can be attributed to the Li/Mg co-intercalation.

The situation is quite different for hybrid Mg-Li cells with a TiS_2 positive electrode.[7] Here, Mg-intercalation into the material is negligible, corresponding to less than 10% of the capacity available in Li- or hybrid Mg-Li batteries. Therefore, Li-insertion represents the main reaction process. The hybrid cell showed no capacity loss for 100 cycles at 1C with Coulombic efficiency of 99.9%, while a control cell with a Li-metal anode only retained 30% of its original capacity with Coulombic efficiency less than 90%. As a reason, it was pointed out that the capacity decay in the Li-cell with TiS_2 was because of the failure of Li anode due to a dendrite growth instead of the degradation of TiS_2 cathode.

The role of the electrolyte composition, namely the concentration of APC, for the resulting performance (cell polarization and capacity retention), was evaluated in case of the $LiCrTiO_4$ spinel,[55] which served as a positive electrode in Mg-Li batteries. Here, only Li-ions can be intercalated into the material as well. It was shown that the ionic conductivity of the electrolyte yields a maximum as the APC amount varies, while the capacity decreases significantly if the concentration of LiCl is reduced from 1 M to 0.1 M while keeping the optimum APC concentration. However, it is worth noting that the reported long-term cycling behavior of $LiCrTiO_4$ in the Mg-Li batteries is less stable than in conventional Li-cells with a carbonate-based electrolyte[57] at similar currents.

In the case of TNO, our work convincingly shows the advantages of the hybrid Mg-Li concept over the conventional Li-battery regarding long-term cycling at low and very high current densities and at elevated temperatures. The reasons for this are manifold.

As we recognized previosly,[19] at a low current density, the long-term cycling of TNO in Mg-Li batteries results in a more stable behavior than in Li-batteries. Under these conditions, a smooth Li-deposition on the Li-foil without noticeable “dead” Li-dendrites must be expected for the Li-only control experiment. A more proper $MgCl_2$/LiCl-containing cathode-electrolyte interface (CEI) formed on the TNO-side in the Mg-Li battery, in contrast to the CEI mostly containing organic carbonates in the Li-battery, was supposed as the main reason for the observed superior cycling. A beneficial $MgCl_2$/LiCl-containing CEI led to decreasing of the Mg-Li cell polarization upon cycling whereas the polarization of the Li-cell rose. At the same time, as TNO exhibits a large part of a pseudocapacitive contribution to the charge storage, it represents an outstanding candidate for an ultra-fast cycling. Moreover, since our DFT calculations unambiguously showed thermodynamic preference of the Li- over the Mg-insertion in TNO, the material maintains its ability for the ultra-fast cycling behavior, because a sluggish

bulk Mg-diffusion is avoided. Although *operando* XRD studies displayed differences in lattice parameters during the insertion process into TNO in Li- and Mg-Li batteries, pointing to some Mg-co-insertion, estimated to be about 20 % according to the *post mortem* TEM analysis, this co-insertion does not deteriorate the cycling behavior with time. We believe the co-insertion to be caused by a reduction of the activation energy of Mg insertion by preceding Li ions, as described in the literature for the Mo_6S_8 material.[43]
Finally, similar to the TiS_2 system in hybrid Mg-Li cells,[7] we confirm the higher stability of the Mg-anode in the APC-LiCl electrolyte over the Li-anode in carbonate-based electrolytes, even for 2000 cycles and 60 °C.

CONCLUSIONS

We showed a very stable long-term cycling of nanoscale $TiNb_2O_7$ as a cathode in hybrid Mg-Li batteries with a Mg-anode and an APC electrolyte with LiCl as a Li-source in the temperature range 25-60 °C. Three parameters facilitate this stable behavior which is superior to analogous Li-batteries with TNO and a Li-anode: *i*) the favorable cathode-electrolyte interface (CEI) containing $MgCl_2$/LiCl, which was observed in the previous work,[19] *ii*) the smooth, dendrite-free and fast Mg deposition/stripping in the APC + LiCl electrolyte up to at least 60 °C, and *iii*) the open TNO structure in combination with nanoscale particles, supporting a very high pseudocapacitive contribution to the storage mechanism. A co-intercalation of Mg of about 25 % into microscale TNO at a low current density of 7.75 mA g^{-1}, and about 15% at 1160 mA g^{-1} into nanoscale TNO was detected after long-term cycling using *post mortem* EDS analysis.

Interestingly, the capacity of the Mg-Li battery with TNO shows a much stronger temperature dependence than of the Li-battery with TNO: a difference in capacities of 100 mAh g^{-1} at 1.55 A g^{-1} between 25 °C and 60 °C was detected for the Mg-Li battery, while only nearly of 40 mAh g^{-1} for the Li battery. Moreover, whereas cell polarization upon cycling decreases (at 25 °C) or remains nearly constant (at 60 °C) in case of the hybrid Mg-Li battery, it increases with cycling in case of the Li-battery. Further studies of hybrid Mg-Li batteries at elevated temperatures are needed to understand their outstandingly stable behavior.

ACKNOWLEDGEMENT

We would like to acknowledge Haneen Albukai (IFW Dresden) for assistance with electrochemical experiments. This project has benefitted from the European Union and the Free State of Saxony under the TTKin project (SAB Grant No. 100225299).

Supporting Information

Supporting information file contains nitrogen physisorption isotherms for the micro- and nanoscale TNO samples, TEM micrographs of TNO (micro- and nanoscale) after electrochemical treatment, electrochemical performance of nanoscale TNO, dry-pressed on stainless steel mesh, in hybrid Mg-Li cells at different current densities, and a table with calculated total amounts of Li and Mg in the electrolyte in hybrid Mg-Li cells.

REFERENCES

(1) Yuan, X.; Ma, F.; Zuo, L.; Wang, J.; Yu, N.; Chen, Y.; Zhu, Y.; Huang, Q.; Holze, R.; Wu, Y.; van Ree, T. Latest Advances in High-Voltage and High-Energy-Density Aqueous Rechargeable Batteries *Electrochem. Energ. Rev. 2020.*

(2) You, C.; Wu, X.; Yuan, X.; Chen, Y.; Liu, L.; Zhu, Y.; Fu, L.; Wu, Y.; Guo, Y.-G.; van Ree, T. Advances in Rechargeable Mg Batteries *J. Mater. Chem. A 2020,8, 25601-25625.*

(3) Cheng, Y.; Shao, Y.; Zhang, J.-G.; Sprenkle, V. L.; Liu, J.; Li, G. High Performance Batteries Based on Hybrid Magnesium and Lithium Chemistry *Chem. Commun. 2014, 50, 9644–9646.*

(4) Cho, J.-H.; Aykol, M.; Kim, S.; Ha, J.-H.; Wolverton, C.; Chung, K. Y.; Kim, K.-B.; Cho, B.-W. Controlling the Intercalation Chemistry to Design High-Performance Dual-Salt Hybrid Rechargeable Batteries *J. Am. Chem. Soc. 2014, 136, 16116–16119.*

(5) Fu, Q.; Azmin, R.; Sarapulova, A.; Mikhailova, D.; Dsoke, S.; Missiul, A.; Trouillet, V.; Knapp, M.; Bramnik, N.; Ehrenberg, H. Electrochemical and Structural Investigations of Different Polymorphs of TiO_2 in Magnesium and Hybrid Lithium/Magnesium Batteries *Electrochim. Acta 2018, 277, 20–29.*

(6) Zhang, Y.; Xie, J.; Han, Y.; Li, C. Dual-Salt Mg-Based Batteries with Conversion Cathodes *Adv. Funct. Mater. 2015, 25, 7300–7308.*

(7) Yoo, H. D.; Liang, Y.; Li, Y.; Yao, Y. High Areal Capacity Hybrid Magnesium–Lithium-Ion Battery with 99.9% Coulombic Efficiency for Large-Scale Energy Storage *ACS Appl. Mater. Interfaces 2015, 7, 7001–7007.*

(8) Shannon, R. D. Revised Effective Ionic Radii and Systematic Studies of Interatomic Distances in Halides and Chalcogenides *Acta Crystallogr. Sect. A 1976, 32, 751–767.*

(9) Yao, H.-R.; You, Y.; Yin, Y.-X.; Wan, L.-J.; Guo, Y.-G. Rechargeable Dual-Metal-Ion Batteries for Advanced Energy Storage *Phys.Chem.Chem.Phys. 2016, 18, 9326-9333.*

(10) Ichitsubo, T.; Okamoto, S.; Kawaguchi, T.; Kumagai, Y.; Oba, F.; Yagi, S.; Goto, N.; Doi, T.; Matsubara, E. Toward "Rocking-Chair Type" Mg–Li Dual-Salt Batteries *J. Mater. Chem. A 2015, 3, 10188–10194.*

(11) Wadsley, A. D. Mixed Oxides of Titanium and Niobium. I. *Acta Cryst. 1961, 14, 660-664.*

(12) Guo, B.; Yu, X.; Sun, X.-G.; Chi, M.; Qiao, Z.-A.; Liu, J.; Hu, Y.-S., Yang, X.-Q., Goodenough, J. B.; Dai, S. A Long-Life Lithium-Ion Battery with a Highly Porous $TiNb_2O_7$ Anode for Large-Scale Electrical Energy Storage *Energy Environ. Sci. 2014, 7, 2220–2226.*

(13) Griffith, K. J.; Seymour, I. D.; Hope, M. A. Butala, M. M.; Lamontagne, L. K.; Preefer, M. B.; Koçer, C. P.; Henkelman, G.; Morris, A. J.; Cliffe, M. J.; Dutton, S. E.; Grey, C. P. Ionic and Electronic Conduction in $TiNb_2O_7$ *J. Am. Chem. Soc. 2019, 141, 16706−16725*

(14) Li, S.; Cao, X.; Schmidt, C. N.; Xu, Q.; Uchaker, E.; Pei, Y.; Cao, G. $TiNb_2O_7$/Graphene Composites as High-Rate Anode Materials for Lithium/Sodium Ion Batteries *J. Mater. Chem. A*, *2016, 4, 4242-4251.*

(15) Adams, S.; Swenson, J. Migration Pathways in Ag-Based Superionic Glasses and Crystals Investigated by the Bond Valence Method *Phys. Rev. B 2000, 63, 054201.*

(16) Momma, K.; Izumi, F. VESTA 3 for Three-Dimensional Visualization of Crystal, Volumetric and Morphology Data *J. Appl. Crystallogr. 2011, 44, 1272−1276.*

(17) Han, J.-T.; Huang, Y.-H.; Goodenough,J. B. New Anode Framework for Rechargeable Lithium Batteries *Chem. Mater. 2011, 23, 2027–2029.*

(18) Tang, K.; Mu, X.; van Aken, P. A.; Yu, Y.; Maier, J. "Nano-Pearl-String" $TiNb_2O_7$ as Anodes for Rechargeable Lithium Batteries *Adv. Energy Mater. 2013, 3, 49–53.*

(19) Maletti, S.; Herzog-Arbeitman, A.; Oswald, S.; Senyshyn, A.; Giebeler, L.; Mikhailova, D. $TiNb_2O_7$ and VNb_9O_{25} of ReO_3 Type in Hybrid Mg-Li Batteries: Electrochemical and Interfacial Insights *J. Phys. Chem. C 2020, 124, 46, 25239–25248.*

(20) Holder, C. F.; Schaak, R. E. Tutorial on Powder X-ray Diffraction for Characterizing Nanoscale Materials *ACS Nano 2019, 13, 7359-7365.*

(21) Yogamalar, R.; Srinivasan, R.; Vinu, A.; Ariga, K.; Bose, A. C. X-Ray Peak Broadening Analysis in ZnO Nanoparticles *Solid State Commun. 2009, 149, 1919-1923.*

(22) Fraunhofer, J. Bestimmung des Brechungs und Farbzerstreuungsvermögens Verschiedener Glasarten *Gilberts Annalen der Physik 1817, 56, 193-226.*

(23) Brunauer, S.; Emmett, P.; Teller, E. Adsorption of Gases in Multimolecular Layers *J. Am. Chem. Soc. 1938, 60, 303-319.*

(24) Thommes, M. Physical Adsorption Characterization of Nanoporous Materials *Chem. Ing. Tech. 2010, 82, 1059-1073.*

(25) Ravikovitch, P. I.; Neimark, A. V. Density Functional Theory Model of Adsorption on Amorphous and Microporous Silica Materials *Langmuir 2006, 22, 11171-11179.*

(26) Herklotz, M.; Weiss, J.; Ahrens, E.; Yavuz, M.; Mereacre, L.; Kiziltas-Yavuz, N.; Draeger, C.; Ehrenberg, H.; Eckert, J.; Fauth, F.; Giebeler, L.; Knapp, M. A Novel High-Throughput Setup for In Situ Powder Diffraction on Coin Cell Batteries *J. Appl. Cryst. 2016, 49, 340-345.*

(27) Roisnel, T.; Rodríguez-Carvajal, J. WinPLOTR: A Windows Tool for Powder Diffraction Patterns Analysis *Mater. Sci. Forum 2001, 378–381, 118–123.*

(28) Kresse, G.; Furthmüller, J. Efficient Iterative Schemes for Ab Initio Total-Energy Calculations Using a Plane-Wave Basis Set *Phys. Rev. B 1996, 54, 11169.*

(29) Kresse, G.; Furthmüller, J. Efficiency of Ab-Initio Total Energy Calculations for Metals and Semiconductors Using a Plane-Wave Basis Set *Comput. Mater. Sci. 1996, 6, 15.*

(30) Kresse, G.; Joubert, D. From Ultrasoft Pseudopotentials to the Projector Augmented-Wave Method *Phys. Rev. B 1999, 59, 1758.*

(31) Koepernik, K.; Eschrig, H. Full-Potential Nonorthogonal Local-Orbital Minimum-Basis Band-Structure Scheme *Phys. Rev. B 1999, 59, 1743.*

(32) Perdew, J. P.; Burke, K.; Ernzerhof, M. Generalized Gradient Approximation Made Simple *Phys. Rev. Lett. 1996, 77, 3865.*

(33) Gasperin, M. Affinement de la Structure de $TiNb_2O_7$ et Répartition des Cations *J. Solid State Chem. 1984, 53, 144.*

(34) Catti, M.; Pinus, I.; Knight, K. Lithium Insertion Properties of $Li_xTiNb_2O_7$ Investigated by Neutron Diffraction and First-Principles Modelling *J. Solid State Chem. 2015, 229, 19–25.*

(35) Urban, A.; Seo, D.-H.; Ceder, G. Computational Understanding of Li-ion Batteries *npj Comput. Mater. 2016, 2, 16002.*

(36) Newville, M. Fundamentals of XAFS, Revision 1.7, *University of Chicago: Chicago, IL, 2004*

(37) Vitova, T.; Mangold, S.; Paulmann, C.; Gospodinov, M.; Marinova, V.; Mihailova, B. X-Ray Absorption Spectroscopy of Ru-Doped Relaxor Ferroelectrics with a Perovskite-Type Structure *Phys. Rev. B 2014, 89, 144112.*

(38) Poltavets, V. V.; Croft, M.; Greenblatt, M. Charge Transfer, Hybridization and Local Inhomogeneity Effects in $Na_xCoO_2{\cdot}yH_2O$: An X-Ray Absorption Spectroscopy Study *Phys. Rev. B 2006, 74, 125103.*

(39) Ise, K.; Morimoto, S.; Harada, Y.; Takami, N. Large Lithium Storage in Highly Crystalline $TiNb_2O_7$ Nanoparticles Synthesized by a Hydrothermal Method as Anodes for Lithium-Ion Batteries *Solid State Ionics 2018, 320, 7–15.*

(40) Augustyn, V.; Come, J.; Lowe, M. A.; Kim, J. W.; Taberna, P.-L.; Tolbert, S. H.; Abruña, D.; Simon, P.; Dunn, B. High-Rate Electrochemical Energy Storage through Li^+ Intercalation Pseudocapacitance *Nat. Mater. 2013,12, 518–522.*

(41) Yu, H.; Lan, H.; Yan, L.; Qian, S.; Cheng, X.; Zhu, H.; Long, N.; Shui, M.; Shu, J. $TiNb_2O_7$ Hollow Nanofiber Anode with Superior Electrochemical Performance in Rechargeable Lithium Ion Batteries *Nano Energy 2017, 38, 109–117.*

(42) Gupta, A.; Shim, S.; Issah, L.; McKenzie, C.; Stone, H. A. Diffusion of Multiple Electrolytes Cannot be treated Independently: Model Predictions with Experimental Validation *Soft Matter 2019, 15, 9965-9973.*

(43) Li, H.; Okamoto, N. L.; Hatakeyama, T.; Kumagai, Y.; Oba, F.; Ichitsubo, T. Fast Diffusion of Multivalent Ions Facilitated by Concerted Interactions in Dual-Ion Battery Systems *Adv. Energy Mater. 2018, 8, 1801475.*

(44) Mehrer, H. Diffusion in Solids: Fundamentals, Methods, Materials, Diffusion-Controlled Processes *Springer Series in solid state science 155, 2007.*

(45) Jiang, Y. J.; Liu, J. Definitions of Pseudocapacitive Materials: A Brief Review *Energy Environ. Mater. 2019, 2, 30–37.*

(46) Wang, X.; Shen, G. Intercalation pseudo-capacitive $TiNb_2O_7$@carbon Electrode for High-Performance Lithium Ion Hybrid Electrochemical Supercapacitors with Ultrahigh Energy Density *Nano Energy 2015, 15, 104–115.*

(47) Bird, R. B.; Stewart, W. E.; Lightfoot, E. N. Transport Phenomena. *John Wiley & Sons 1976*

(48) Babu, B.; Shaijumon, M. M. Studies on Kinetics and Diffusion Characteristics of Lithium Ions in $TiNb_2O_7$ *Electrochim. Acta 2020, 345, 136208.*

(49) Campion, C. L.; Li, W.; Lucht, B. L. Thermal Decomposition of $LiPF_6$-Based Electrolytes for Lithium-Ion Batteries *J. Electrochem. Soc. 2005, 152, A2327.*

(50) Wang, Q.; Sun, J.; Yao, X.; Chen, C. Thermal Behavior of Lithiated Graphite with Electrolyte in Lithium-Ion Batteries *J. Electrochem. Soc. 2006, 153, A329.*

(51) Aurbach, D.; Zinigrad, E.; Cohen, Y.; Teller, H. A Short Review of Failure Mechanisms of Lithium Metal and Lithiated Graphite Anodes in Liquid Electrolyte Solutions *Solid State Ionics 2002,148, 405-416.*

(52) Zhang, Y.; Zhong, Y.; Shi, Q.; Liang, S.; Wang, H. Cycling and Failing of Lithium Metal Anodes in Carbonate Electrolyte *J. Phys. Chem. C 2018, 122, 21462–21467.*

(53) Matsui, M. Study on Electrochemically Deposited Mg Metal *J. Power Sources 2011, 196, 7048-7055.*

(54) Pei, C.; Xiong, F.; Sheng, J.; Yin, Y.; Tan, S.; Wang, D.; Han, C.; An, Q.; Mai, L. VO_2 Nanoflakes as the Cathode Material of Hybrid Magnesium−Lithium-Ion Batteries with High Energy Density *ACS Appl. Mater. Interfaces 2017, 9, 17060−17066.*

(55) Yao, Y.; Zhang, L.; Bie, X.; Chen, H.; Wang, C.; Du, F.; Chen, G. Exploration of Spinel $LiCrTiO_4$ as Cathode Material for Rechargeable Mg-Li Hybrid Batteries *Chem. Eur. J. 2017,23,17935-17939.*

(56) Cen, Y.; Liu, Y.; Zhou, Y.; Tang, L.; Jiang, P.; Hu, J.; Xiang, Q.; Hu, B.; Xu, C.; Yu, D.; Chen, C. Spinel $Li_4Mn_5O_{12}$ as 2.0 V Insertion Materials for Mg-Based Hybrid Ion Batteries *ChemElectroChem 2020, 7, 1115–1124.*

(57) Aravindan, V.; Ling, W. C.; Madhavi, S. $LiCrTiO_4$: A High-Performance Insertion Anode for Lithium-Ion Batteries *ChemPhysChem 2012, 13, 3263 – 3266.*

Graphical Abstract